CONTRAST MEDIA & MOLECULAR IMAGING

Received: 22 November 2010, Revised: 8 June 2011, Accepted: 17 June 2011, Published online in Wiley Online Library: 2012

(wileyonlinelibrary.com) DOI: 10.1002/cmmi.471

Efficacy of positive contrast imaging techniques for molecular MRI of tumor angiogenesis

M. Wolters[a,c], M. Oostendorp[a,b,f], B. F. Coolen[c], M. J. Post[a,d], J. M. H. Janssen[e], G. J. Strijkers[c], M. E. Kooi[a,b], K. Nicolay[c] and W. H. Backes[a,b]*

Superparamagnetic iron oxide particles (SPIOs) are promising contrast agents for molecular MRI. To improve the *in vivo* detection of iron-based contrast media, positive contrast imaging techniques have been developed. Here, the efficacy of two positive contrast techniques, white marker and susceptibility gradient mapping (SGM), were evaluated for molecular MRI of tumor angiogenesis and compared with conventional negative contrast gradient echo (GE) imaging. *In vitro*, cylindrical phantoms containing varying iron oxide concentrations were used to measure the response of positive contrast techniques. *In vivo*, tumor bearing mice were used as a model for tumor angiogenesis. Mice were injected with unlabeled SPIOs ($n = 5$) or SPIOs labeled with cyclic NGR peptide (cNGR) ($n = 5$), which homes specifically to angiogenic microvessels. Pre- and post-contrast GE and white marker images were acquired. Subsequently, SGM images and R_2^* maps were calculated. For image analysis, the contrast-to-noise ratio (CNR) and the percentage of enhanced voxels (EVs) in the tumor rim and core were calculated. *In vitro*, the linear increases in MRI signal response for increasing iron oxide concentration were much stronger for SGM than white marker. *In vivo*, the CNR of GE, white marker and SGM imaging was 5.7, 1.2 and 6.2, respectively, with equal acquisition times. Significant differences in the percentage of EVs between the tumor rim and core were found using R_2^* mapping, GE and SGM ($p < 0.05$). The two contrast agents had significantly different percentages of EVs by R_2^* mapping and SGM in the rim ($p < 0.001$). The *in vivo* efficacy of white marker and SGM was evaluated for molecular MRI relative to GE imaging and R_2* mapping. Only SGM, and not white marker, can be used to transfer the negative contrast from targeted SPIOs in a positive contrast signal without loss of CNR. Copyright © 2012 John Wiley & Sons, Ltd.

Keywords: positive contrast; molecular MRI; NGR; SPIO; white marker; susceptibility gradient mapping; angiogenesis

1. INTRODUCTION

Molecular imaging involves the detection of sparse biomarkers and requires high sensitivity of the contrast agent and imaging technique (1,2). MRI is a highly desirable modality for molecular imaging as it provides high spatial resolution and excellent soft tissue contrast. However, the inherently low sensitivity of MRI for the detection of contrast agents makes imaging of sparse biomarkers of diseases more difficult compared with nuclear or optical techniques. To obtain sufficient T_1-weighted image contrast, relatively large particles (e.g. polymers, liposomes, micelles) are usually administered, carrying a high payload of gadolinium (3–5). Alternatively, iron oxide particles can be applied to generate T_2 and, in particular, T_2^*-weighted contrast. These susceptibility contrast agents are known for their good sensitivity at low particle concentrations (2). An example of molecular MRI of angiogenesis using a targeted ultra small superparamagnetic iron oxide (USPIO)-based contrast agent was provided by Zhang *et al.* (6). As the accumulation of iron oxides in tissue generally results in reduced T_2^* relaxation times, the signal decrease induced by the iron-particles (i.e. negative contrast) can be difficult to discern from intrinsically hypointense or heterogeneous background tissue, especially at higher field strengths.

* *Correspondence to: W. H. Backes, Maastricht University Medical Center, P. Debyelaan 25, 6229 HX Maastricht, the Netherlands.*
E-mail: w.backes@mumc.nl

a *M. Wolters, M. Oostendorp, M. J. Post, M. E. Kooi, W. H. Backes*
Cardiovascular Research Institute Maastricht, Maastricht University Medical Center, Maastricht, the Netherlands

b *M. Oostendorp, M. E. Kooi, W. H. Backes*
Department of Radiology, Maastricht University Medical Center, Maastricht, the Netherlands

c *M. Wolters, B. F. Coolen, G. J. Strijkers, K. Nicolay*
Biomedical NMR, Department of Biomedical Engineering, Eindhoven University of Technology, Eindhoven, the Netherlands

d *M. J. Post*
Department of Physiology, Maastricht University Medical Center, Maastricht, the Netherlands

e *J. M. H. Janssen*
Department of Pathology, Maastricht University Medical Center, Maastricht, the Netherlands

f *M. Oostendorp*
Laboratory of Clinical Chemistry and Haematology, University Medical Centre Utrecht, the Netherlands

To overcome this issue, several positive contrast techniques have been developed which generate hyperintensities in the vicinity of iron oxide nanoparticles. These techniques can be divided into three groups: gradient sensitive techniques (7,8), frequency sensitive techniques (9–11) and post-processing techniques (12,13). The present study evaluates two positive contrast techniques, a gradient sensitive technique, white marker (7) and a post-processing technique, susceptibility gradient mapping (SGM) (12). The theoretical background of white marker and SGM is summarized in Fig. 1.

The main objective of this study was to compare the two positive contrast techniques with traditional gradient echo (GE) imaging for molecular MRI of tumor angiogenesis using targeting SPIOs. The feasibility and *in vivo* application of positive-contrast MRI has been demonstrated previously (7,12,14,15). However, so far it has remained unclear whether this can be used for molecular imaging and how the contrast effect compares with negative contrast imaging. The current study presents the applicability of white marker and SGM to depict uptake in angiogenesis exhibiting tumors using targeted iron oxide nanoparticles. Both techniques were first optimized and compared in phantoms and then evaluated in tumor-bearing mice using cyclic NGR (cNGR) tripeptide-labeled iron oxide particles that home to activated endothelial cells of angiogenic blood vessels. The cNGR peptide has a high affinity for CD13, which is a well-known angiogenic marker (16–21). This peptide has already successfully been used in experimental molecular MRI studies of angiogenesis in tumors and in the heart (22,23).

2. METHODS AND MATERIALS

2.1. Phantom MRI experiments

To test and optimize the different MRI acquisition techniques, two phantoms were used: (1) a single iron oxide cylinder phantom to optimize acquisition and imaging techniques; and (2) a phantom with multiple iron oxide cylinders to determine the signal response of positive contrast techniques on different iron oxide concentrations.

For the first phantom, the single cylinder phantom, a cylindrical tube (diameter 30 mm; length 70 mm) was filled with 2% agarose gel. The center of this phantom contained a 3 mm cylindrical core filled with 2% agarose gel containing 0.15 mmol Fe l^{-1} (Resovist 0.5 mol Fe l^{-1}, Schering). Imaging was performed on a 7.0 T horizontal bore MRI system (Bruker Avance II Biospec 70/30 USR, Ettlingen, Germany) equipped with a BGA12 mini imaging gradient system (maximum gradient strength 400 mT m^{-1}; slew rate, 4000 T m^{-1} s^{-1}) and a quadrature volume resonator (inner diameter 82 mm). The cylindrical axis of the phantom was

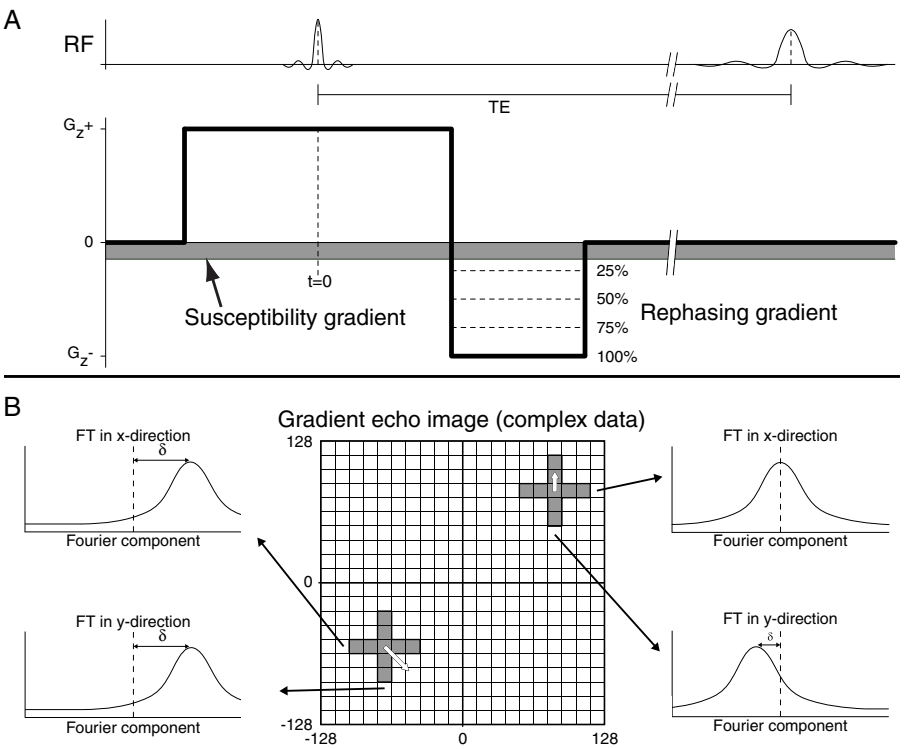

Figure 1. (A) Slice selection gradient (G_z), the susceptibility gradient and the RF signal (RF) of the white marker (7) sequence. For conventional gradient echo (GE) imaging, the dephasing of spins in the selected slice is compensated for by the rephrasing gradient of equal strength and opposite direction. The presence of iron-oxide particles will induce field inhomogeneities, which is represented by the susceptibility gradient (gray). Owing to this susceptibility gradient, the dephasing of the spins will be altered and will not be completely rephrased by the original slice selection gradient, which will lead to signal loss. For white marker, the strength of the rephasing gradient can be adjusted (0–100%) to compensate for the additional dephasing effect of the iron oxide-induced susceptibility gradient. The correct rephasing depends on the strength of the rephasing gradient, the susceptibility gradient, and the echo time. (B) The principle of SGM (12). The SGM image is calculated from the complex pixel values of a GE image. A sliding window of five pixels samples the complex data of the GE image. Subsequently, these data samples are Fourier-transformed to a short-term *k*-space. The susceptibility gradient (white arrow), is determined from the shift δ of the maximum in the Fourier spectrum relative to the spatial frequency $k = 0$. This shift is proportional to the strength of the susceptibility gradient and was assigned to the center position of the sliding window in the SGM image. With SGM, it is possible to slide a window in two or three directions to obtain a 2D or 3D susceptibility vector, respectively.

placed vertically in the (horizontal) magnet bore and perpendicular to the magnetic field B_0. In this orientation, a paramagnetic cylinder will induce susceptibility gradients perpendicular to the cylinder and the susceptibility gradient parallel to the cylinder is minimized. This phantom, with a well-known susceptibility geometry, was used to optimize the imaging techniques. For image acquisition, a series of conventional GE sequences ($TE = 3.5$, 7, 10, 15, 25 ms, $TR = 750$ ms, and Flip Angle FA = 40°) and a series of white marker sequences (TE = 5 ms, TR = 750 ms, FA = 40°, rephasing 100, 75, 50, 25, 0%) were applied. The white marker sequence is a GE sequence with an altered rephasing gradient in the slice selection (Fig. 1A); 100% rephasing represents a complete rephasing and is therefore equal to a conventional GE acquisition. 25% rephasing is a quarter of the strength of the rephasing gradient of a GE acquisition. For both the white marker and the GE sequences, five 1 mm-thick axial slices with a gap of 1 mm were acquired. The acquired matrix was 256 × 256 and the field of view (FOV) was 30 × 30 mm, resulting in 0.12 × 0.12 mm^2-sized voxels. White marker depicts only positive contrast in the slice direction. Therefore, axial slices (i.e. short-axis sections) are not useful and coronal slices (i.e. long-axis sections) were applied, owing to the minimal susceptibility gradient parallel to the cylinder in this orientation.

For the second phantom, the multiple cylinder phantom, a 30 mm cylindrical tube with nine vertical cylinders, 1 mm in diameter and 10 mm in height, was designed (Fig. 3A and 3B). The cylinders were filled with iron concentrations of 0.0, 0.1, 0.2, 0.3, 0.6, 0.7, 0.8, 0.9 and 1.0 mmol Fe l^{-1}, diluted in saline buffer. For gradient echo imaging, the same setup up was used as for the first phantom experiment. A single 1 mm axial (short-axis) slice was acquired with a conventional GE sequences ($TE = 3.5$, 7, 15 ms, $TR = 750$ ms, and FA = 40°). For white marker 100, 50 and 25% rephasing was applied. For each rephasing value two orthogonal long-axis (one parallel and one perpendicular to B_0) acquisitions were made. Both acquisitions had a matrix of 256 × 256, 64 slices and a voxel size of 0.2 × 0.2 × 0.8 mm^3. The image data of acquisition were interpolated to obtain one reformatted image, i.e. an axial (short-axis) image (pixel size, 0.2 × 0.2 mm^2) as used for the gradient echo acquisition.

2.2. Contrast agent

Streptavidin-coated SPIOs (μMACS™) were obtained from Miltenyi Biotec (Bergisch Gladbach, Germany) (24). The absolute iron concentration in the SPIO solution was 0.28 mg ml^{-1}, as measured using inductively coupled plasma mass spectrometry, which is equivalent to an iron concentration of 5 mM. To measure r_1, r_2 and r_2^* relaxivities, SPIOs were diluted in saline in eight steps to concentrations of 0–0.7 mmol Fe l^{-1}. The R_1, R_2 and R_2^* of each sample were determined using a series of Inversion Recovery IR ($TE = 8.1$ ms; $TR = 10\,000$ s; $TI = 150$, 250, 500, 750, 1000, 1500, 2000, 2500, 3000 and 3500 ms), Spin Echo SE ($TE = 11$, 22, 33, 44, 55, 66, 77, 88, 99, 110, 121 and 132 ms; $TR = 10\,000$) and GE ($TE = 3.9$, 7.5, 10, 15, 20, 25, 30 and 40 ms; $TR = 10\,000$; FA = 40°) acquisitions, respectively. Before acquisition, first- and second-order global shimming was performed. All data were acquired at room temperature.

The cNGR peptide used in this study was biotinylated and could therefore be easily linked to the SPIOs. The iron oxide nanoparticles are able to bind 100 nmol ml^{-1} biotinylated compounds, as indicated by the manufacturer. For the *in vivo* experiment, a dose of 200 μl was prepared. The peptide was dissolved in water and 20 nmol peptide was added to the iron nanoparticles. This resulted in a total dose of approximately 29 μmol Fe kg^{-1} body weight. Unlabeled SPIO contrast agent was used as control.

2.3. Animal model

The animal study was approved by the institutional animal welfare committee. Human colorectal adenocarcinoma cells (1.5–3.0 × 10^6; LS174T; American Type Culture Collection CL-188) were subcutaneously injected in one flank of 12-week-old male Swiss nu/nu mice (Charles River Laboratories, L'Arbresle cedex, France). Mice were subjected to MRI when the tumor volume was approximately 1 cm^3, which was 14 days after LS174T injection. For *in vivo* MRI, mice were anesthetized using 1.5–2.0% isoflurane (Abbott Laboratories Ltd Queensborough, UK) in medical air and were placed in prone position in a dedicated animal holder with a built-in mask for anesthesia gas supply. An infusion line was placed in the jugular vein for contrast agent administration during MRI. A heating pad was placed over the mice to maintain normothermic conditions. Respiration rate and body temperature were continuously monitored via a balloon sensor and a rectal temperature probe, respectively, interfaced to an MR compatible small animal monitoring system (SA Instruments Inc., Stony Brook, NY, USA). Mice were randomly selected for injection with either cNGR-labeled SPIOs or unlabeled SPIOs. For both contrast agent groups, five mice were included. The investigator was blinded for the administered contrast agent. After the MRI experiment, all mice were euthanized by exsanguination and perfusion fixed with 2% glutaraldehyde. Tumors were excised, sliced in approximately 1 mm slices corresponding to the MRI geometry and conserved in 2% glutaraldehyde for histology.

2.4. *In vivo* MRI experiment

For animal experiments, the 7.0 T MRI system was equipped with a BGA6-S microimaging gradient system (maximum gradient strength, 1000 mT m^{-1}; slew rate, 11250 T m^{-1} s^{-1}) and a quadrature volume resonator (inner diameter, 35 mm). Pre- and post-contrast images were acquired with a FOV of 30 × 30 mm^2, 192 × 256 acquisition matrix, 256 × 256 reconstruction matrix, 0.12 × 0.12 mm^2 voxel size and 1 mm slice thickness. In the tumor, six to eight axial slices were planned depending on the dimensions and orientation of the tumor. The order of the scans was randomized for each animal and consisted of a T_2-weighted spin echo sequence for tumor localization (TE = 30 ms and $TR = 3500$ ms), a GE series ($TE = 2.9$, 6, 10, 15, 25 ms, $TR = 750$ ms and FA = 40°) and a white marker series ($TE = 5$ ms, $TR = 750$ ms, rephasing 50, 25 and 0%). To determine the plasma half-life of the contrast medium, a dynamic GE series ($TE = 4.0$ ms, $TR = 7.0$ ms, 6.7 s per dynamic phase, FOV = 30 × 30 mm^2, matrix = 64 × 64) was acquired with 100 dynamic phases, and 200 μl of contrast agent was administered after the twentieth dynamic phase inside the magnet. Post-contrast imaging was started 2 min after the dynamic scan.

2.5. Histology

The fixed tumor tissue was processed overnight in the Tissue-Tek VIP apparatus (Sakura, Zoeterwoude, the Netherlands) where it was dehydrated and permeabilized for paraffin perfusion. After paraffin perfusion, the tissues were blocked in paraffin and

sections (4 μm) were cut on a microtome (Leica Microsystems, Nussloch, Germany). Iron-staining was performed on tissue sections according to Perls, with solution A containing 2 g Potassium Ferrocyanide(II) (Merck, Darmstadt, Germany) in 100 ml aqua dest, and solution B being 2% HCl (Merck, Darmstadt, Germany). Before staining, equal volumes of solutions A and B were filtrated through a paper filter (Schleicher&Schuell, Dassel, Germany). Tissue sections were deparaffinized in xylene (Merck, Darmstadt, Germany) and rehydrated in a series of alcohol (100 → 0%). Next, the slides were incubated in Perls staining solution for 30 min and counterstained with Nuclear Fast Red (Klinipath, Duiven, the Netherlands) for 5 min. After rinsing in aqua dest, the slides were dehydrated in a series of alcohol (0 → 100%) and xylene and mounted on a microscope glass with Entellan (Merck, Darmstadt, Germany). Slides were examined on a Leica DM3000 microscope equipped with a DFC320 camera.

2.6. Data analysis

R_2^* relaxation rate maps were calculated from the series of five GE acquisitions. The complex image data of these images was subsequently used to compute the SGM images (Fig. 1B). SGM uses a shifting window (size, five voxels) in which Fourier transformation of the complex image data is performed (25). The spectral shift in the obtained Fourier spectrum with respect to the center of the spectrum is proportional to the susceptibility gradient. The spectral shift was determined by calculating the center of mass of the spectrum and was assigned to the center voxel of the shifting window in the calculated SGM image. The SGM image contained two susceptibility gradient vectors originating from the *x*- and *y*-direction of each voxel. The susceptibility gradient in each voxel was calculated by taking the length of the resulting vector.

Regions of interest (ROI) were drawn manually using MRIcro (26). For the single cylinder phantom, two ROIs were drawn, the first in the positive contrast regions and the second in a nonpositive contrast region inside the phantom. The contrast-to-noise ratio (CNR) for SGM, white marker and GE was determined by

$$\mathrm{CNR} = \frac{|S_A - S_B|}{\sigma}$$

where S_A and S_B are the mean values of the ROIs (the positive contrast area and the nonpositive contrast area, respectively) and σ is the standard deviation of the nonpositive contrast ROI. For the multiple cylinder phantom, one ROI was drawn covering the entire cross-section of the tube, nine equally sized ROIs were drawn for the iron oxide cylinders and the direct vicinity, and

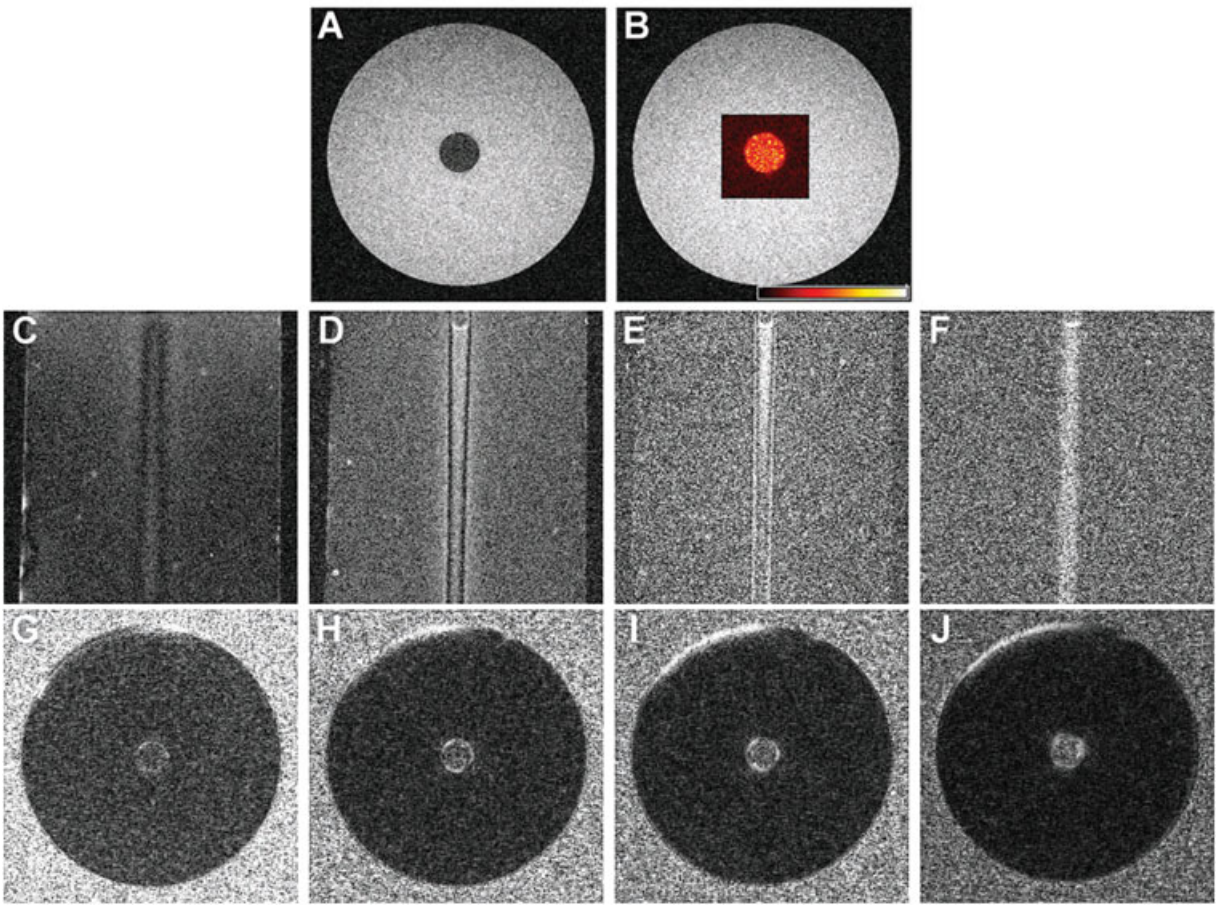

Figure 2. (A) Conventional axial gradient echo image (*TE*, 7 ms) of the cylindrical agarose phantom with an iron oxide-filled core. (B) R_2^* relaxation rate map, range from 0 to 100 s^{-1}. (C–F) Coronal sections of the phantom for the white marker with different percentages of the rephasing gradient strength: 75% (C), 50% (D), 25% (E), and 0% (F). (G–J) SGM images with different *TE* of 3.5 ms (G), 7 ms (H), 10 ms (I) and 15 ms (J). Note that the orientation of the white marker slices is different from those of the GE and SGM images as the cylinder was equally positioned along the B_0 field. The white marker technique is only sensitive to susceptibility gradients in the slice selection direction.

Table 1. CNR values of the cylindrical agarose phantom with iron oxide core, measured for SGM and white marker with different settings

White marker		SGM	
Rephasing (%)	CNR	*TE* (ms)	CNR
0	1.6	3.5	1.6
25	2.3	7	4.2
50	2.2	10	4.9
75	1.8	15	5.3
		25	4.7

one ROI was drawn in the rim of the tube to obtain background signal outside the positive contrast regions. Enhanced voxels (EVs) were selected for each positive contrast technique, which was defined as the 5% voxels with the strongest contrast agent induced signal of the tube. CNR was calculated for each concentration by using only EVs, which were within the ROI (iron oxide cylinder and vicinity). For the *in vivo* images of the different acquisition techniques, ROIs were drawn in the rim and core of each tumor. Again, only EVs were considered during image analysis, which was defined as the 5% voxels with the strongest contrast agent induced signal differences between post- and pre-contrast images. All voxel intensity values from each animal and each group (per contrast agent type) were collected to produce a histogram. From this histogram the 5% most strongly enhanced voxel values were taken. For these voxels, the probability of being part of the nonenhanced background tissue is 5% or less. Increasing this cut-off percentage to 10% did not essentially modify the results of the comparison study. For the *in vivo* measurements, the signal difference $S_A - S_B$ was defined as the mean pixel difference of the post- and pre-contrast images of the EVs. For σ, the standard deviation of the pre-contrast signal in the contralateral nonangiogenic muscle tissue was taken. Comparison of the different imaging techniques was restricted to those acquisitions where cNGR-labeled SPIOs were administered.

2.7. Statistical analysis

First, the number of EVs for rim and core was compared with a nonparametric Wilcoxon signed-rank test and the ratio for unlabeled and cNGR-labeled SPIOs was tested with a nonparametric Mann–Whitney *U*-test. Second, the number of EVs as a function of the distance of the tumor contour was evaluated with spatial linear regression analysis. A significant (negative) correlation would indicate a rim–core difference. The intercept resulting from the regression analysis was used to compare the rim uptake of labeled and unlabeled SPIOs. All statistical tests were performed on the results of R_2^*, SGM and GE using a commercial statistical software package (SPSS 16, SPSS Inc., Chicago, IL, USA). A value of $p < 0.05$ was considered statistically significant.

3. RESULTS

3.1. Phantom MRI experiment

For GE, R_2^* relaxation rate mapping, white marker and SGM, representative images of the single cylinder phantom are presented in Fig. 2. The R_2^* relaxation rate was calculated in an ROI on an axial slice. The R_2^* contrast between the iron oxide-filled cylindrical core and the agarose-filled outer shell of the phantom is visible with this technique (Fig. 2B). For the white marker images, coronal slices were acquired, since the gradient caused by the iron needs to be in the slice direction to generate positive contrast with this technique. The positive contrast is noticeable along the cylinder axis (Fig. 2C–F). For SGM, the strongest positive contrast arises at the interface between the iron-oxide-filled core and the agarose-filled outer shell of the phantom. This is because the SGM technique visualizes the susceptibility gradient, which is only present in the direct vicinity outside the iron oxide core (Fig. 2G–J).

CNR values for the various acquisition techniques for the single cylinder phantom are presented in Table 1. For the positive contrast techniques, the highest CNR of 5.3 was obtained with the SGM sequence with a *TE* of 15 ms. For white marker, the highest CNR of 2.3 was obtained with 25% rephasing.

For the multiple cylinder phantom experiment, the CNR of the SGM images showed a linear relation (highest slope 9.10 ± 0.38 l mmol^{-1} Fe at $TE = 7$ ms, $R_2 = 0.99$) with the iron oxide concentration at various echo times (Fig. 3E). For white marker the most sensitive linear relation (highest slope 0.41 ± 0.17 l mmol^{-1} Fe,

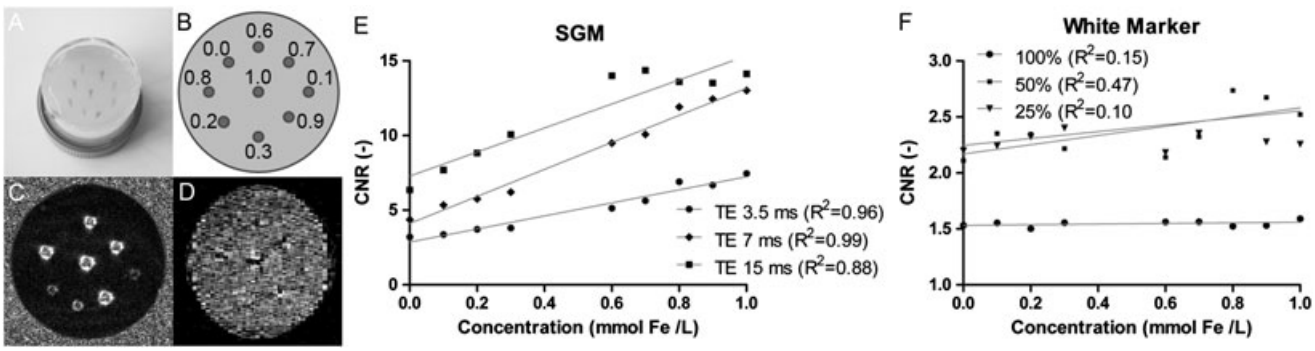

Figure 3. (A) Photograph of the (multi cylinder) phantom with the iron oxide-filled cylinders. (B) Scheme of the iron oxide concentration at each position (in mmol Fe l^{-1}). (C) Axial (short-axis) SGM image (*TE* 15 ms, *TR* 750 ms). Positive contrast is shown in the direct vicinity of the cylinder; at higher iron oxide concentration the positive contrast becomes stronger. (D) Axial (short-axis) white marker image (50% rephasing), obtained by interpolation and reformation of two orthogonally acquired long-axis images. (E, F) CNR of SGM and white marker as function of the concentration for different echo times or rephasing values.

$R_2 = 0.47$) was found for 50% rephasing, with a small positive slope (Fig. 3F).

3.2. Animal experiments

3.2.1. Contrast agent characterization

The relaxivities r_1, r_2 and r_2* at 7.0 T were 1.30 ± 0.13 ($R_2 = 0.951$), 196 ± 9.4 ($R_2 = 0.987$) and 416 ± 11 ($R_2 = 0.996$) $s^{-1}\,mM^{-1}$ Fe, respectively. The hydrodynamic diameter of the SPIO particles was 86.3 nm with a polydispersity index of 0.13, as measured using dynamic light scattering. For cNGR-labeled SPIOs, the plasma half-life was 63.3 ± 13.6 s and for the unlabeled SPIO 64.8 ± 12.1 s, as determined from an exponential fit of the signal decay curve in the aorta.

3.2.2. Positive contrast imaging in tumors

Figure 4 shows representative images of a tumor-bearing mouse injected with cNGR-SPIO contrast agent for the different imaging techniques. For the GE and SGM, but not for white marker images, the effect of contrast uptake is noticeable when pre- and post-contrast images are compared. The post-contrast GE and SGM images show hypointense regions at exactly the same position. An R_2^* post- and pre-contrast subtraction image, ΔR_2^*, was calculated and showed increased relaxations rates in panel

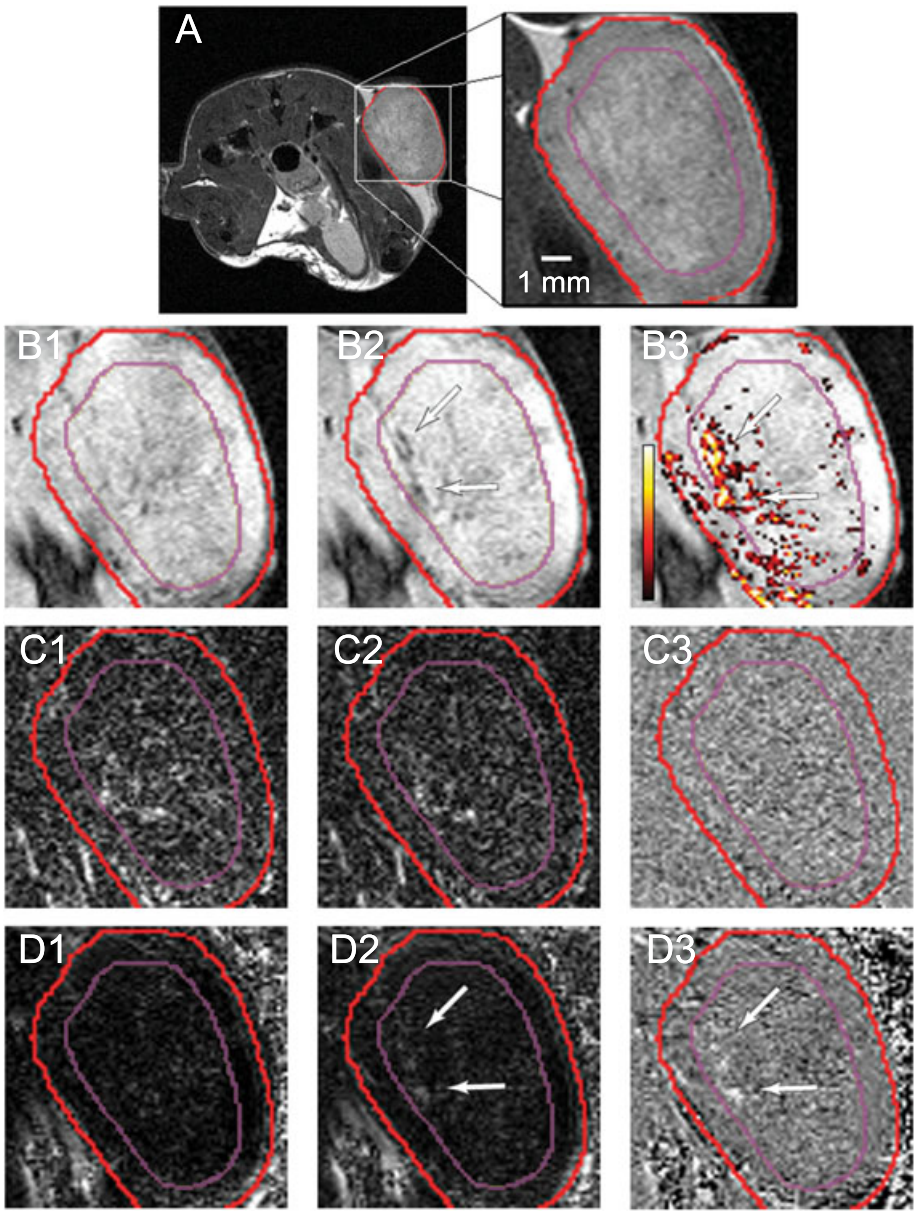

Figure 4. Axial sections through the tumor, where the red line represents the tumor contour and the purple line divides the rim and core section (1 mm-thick rim). (A) A spin echo image that shows the location of the tumor in a mouse of the cNGR-SPIO group. (B1, B2) Pre- and post-contrast GE images, respectively. (B3) ΔR_2^* mapping (post – pre-contrast), color bar range is 0 (black) to 100 (white) s^{-1}. (C1, C2) Pre- and post-contrast white marker images with 0% rephasing, respectively. (C3) ΔWhite marker (post – pre-contrast). (D1, D2) Pre- and post-contrast SGM $TE = 6$ ms, respectively. (D3) ΔSGM image (post – pre-contrast). The arrows show SPIO accumulation in different images.

B3 (Fig. 4). Also the SGM subtraction image, ΔSGM, showed an increased susceptibility gradient in panel D3 (Fig. 4). White marker displayed a weak contrast, which could not be correlated with the hyperintensities of the other techniques.

3.2.3. *Histology*

Perls iron staining was performed on a number of slices of the excised tumors, where the blue coloring indicates iron oxide accumulation. Examination of the slices showed a spatial correspondence with the MRI acquisitions. Blue coloring occurs mainly in the rim and could be related to the contrast enhancement on the *in vivo* post-contrast MRI (Fig. 5).

3.2.4. *Contrast-to-noise ratio*

For SGM and GE images, the highest CNR values in tumor bearing mice were 6.2 ± 0.5 and 5.7 ± 0.9, respectively, whereas the best white marker images had a CNR of 1.2 ± 0.1 (Table 2). The CNR of SGM was slightly higher than for conventional GE images, although it was not significantly different. The CNR of white marker was significantly lower than for SGM and GE ($p < 0.05$).

3.2.5. *Rim and core analysis*

Figure 6 shows a diagram of the percentage of EVs, as determined by the ΔR_2^* measurements, as a function of the distance to the tumor periphery. The mean percentage EVs decreased from 0 to 1 mm distance for both labeled SPIOs and unlabeled SPIOs according to linear regression analysis ($R_2 = 0.97$ for labeled SPIOs and $R_2 = 0.86$ for unlabeled SPIOs). Furthermore, linear regression analysis showed a higher intercept in the percentage of EVs for the cNGR-labeled SPIOs compared with the unlabeled SPIOs ($p < 0.001$), which indicates a significantly higher accumulation of cNGR-labeled SPIOs in the rim compared with the unlabeled SPIOs. The same analysis was performed for SGM ($TE = 6$ ms), which also showed a decrease ($R_2 = 0.95$ for both contrast agents) in EVs as a function of distance and a significantly higher intercept for the cNGR-labeled SPIOs ($p < 0.001$). The percentage of EVs remained approximately constant beyond 1 mm. Therefore, the thickness of the rim was chosen as 1 mm to further evaluate the differences between cNGR and unlabeled SPIOs over the tumor rim and core (22,27,28).

Ligand efficacy was further analyzed by comparing the number of EVs in the 1 mm-thick rim and core for R_2^* mapping, SGM ($TE = 6$ ms) and the GE image ($TE = 6$ ms; Fig. 7). Significantly stronger rim enhancement relative to the core was found for all three techniques and both contrast agents ($p < 0.05$), except for unlabeled SPIOs in the GE images. The stronger enhancement in the rim compared with the core reflects the higher level of angiogenic activity and blood volume typically found in the tumor rim (22,29).

Table 2. *In vivo* CNR values for tumor bearing mice injected with cNGR-labeled SPIOs for GE, white marker and SGM acquisitions with different echo time or rephasing

GE		White marker		SGM	
TE (ms)	CNR	Rephasing (%)	CNR	*TE* (ms)	CNR
3	5.1 ± 0.5	0	1.2 ± 0.1	3	4.9 ± 0.4
6	5.7 ± 0.9	25	1.2 ± 0.1	6	6.2 ± 0.5
10	3.9 ± 0.6	50	1.2 ± 0.1	10	5.7 ± 0.7
15	3.1 ± 0.5			15	4.8 ± 0.7

4. DISCUSSION

4.1. Current findings

In this study, two positive contrast MRI techniques to detect iron oxide contrast agents, white marker and SGM, were compared with GE imaging and R_2^* mapping in cylindrical phantoms and in tumor-bearing mice. In both experiments, SPIOs could be detected with positive contrast techniques. First, the white marker and the SGM technique were optimized for a phantom to obtain the strongest positive contrast between iron-oxide-filled regions and the agarose-filled background. The *in vitro* MRI sensitivity, in terms of signal increase per iron oxide concentration unit, was much higher for SGM than white marker (range 0–1 mmol Fe l^{-1}). Second, *in vivo* experiments with these optimized techniques showed that only SGM, and not white marker, provided positive contrast, which was comparable to R_2^* mapping in terms of signal effect and localization. Third, a stronger uptake of cNGR-labeled SPIOs in the 1 mm-thick tumor rim relative to the core region was observed for SGM and R_2^* mapping. Fourth, both MRI and histology demonstrated accumulation of cNGR-labeled SPIOs mainly in the tumor. Fifth, spatial linear regression analysis showed a significantly higher uptake

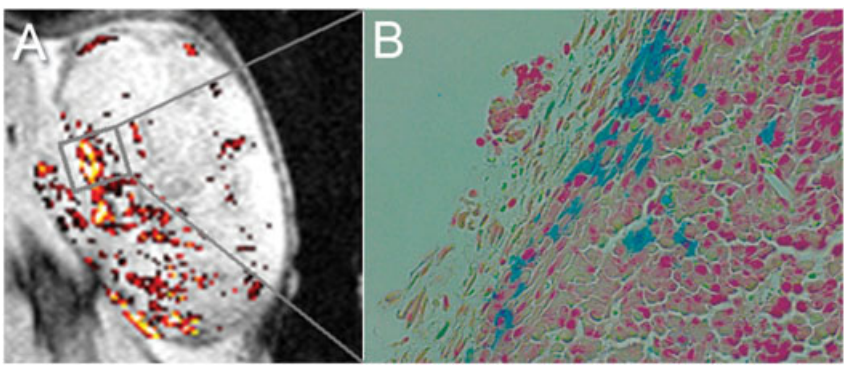

Figure 5. Comparison of contrast-enhanced MRI with histology. The box in the ΔR_2^* mapping (A) shows the location of the corresponding histological tissue section (B). The tumor tissue slice in (B) is stained for iron (Perls blue) and shows iron oxide accumulation in the tumor rim.

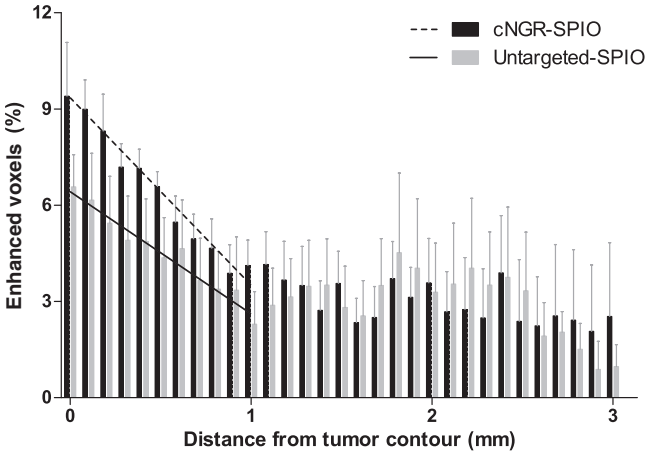

Figure 6. The percentage of EVs versus the distance to the tumor contour with relaxation rate mapping (ΔR_2^*). There is a deceasing trend from 0 to 1 mm. Based on this observation, 1 mm was chosen as the thickness of the rim. Data are presented as means ± standard errors.

of cNGR-labeled SPIOs relative to unlabeled SPIOs in the outermost part of the rim for R_2^* mapping and SGM.

4.2. *In vivo* versus *in vitro* imaging

Different results were found in the *in vivo* and *in vitro* experiments for the positive contrast techniques. In the phantom experiments, SGM achieved the strongest positive contrast at an echo time of 15 ms, whereas *in vivo* the optimal echo time was found to be 6 ms. The differences between these results are probably related to *in vivo* motion artifacts and geometric differences. With an increasing echo time the motion artifacts will also increase. Therefore, the optimal positive contrast for *in vivo* SGM will shift to lower echo times. Furthermore, some artifacts appear outside the ROI in both the pre- and post-contrast SGM images owing to tissue–air interfaces for the intestines and the skin.

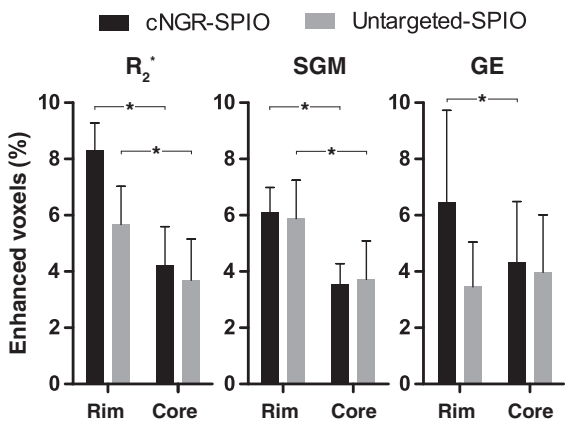

Figure 7. The percentage of EV at optimal settings (SGM and GE: *TE* 6.0 ms) for all techniques. The percentage of EVs is given for rim and core and for both contrast agent groups. Significant differences were found between rim and core for all three techniques and both contrast agents (*$p < 0.05$), except for untargeted-SPIO in the GE image. Data are presented as means ± standard errors.

White marker showed positive contrast in the phantom, whereas hardly any contrast was found *in vivo*. The differences between *in vivo* CNR and *in vitro* CNR for white marker are possibly due to differences in the induced susceptibility gradient of the iron oxide. The strength of the magnetic perturbation depends on a number of parameters, including magnetic properties of the iron particles and shape and dimension of the iron particle distribution. The magnetic field perturbation of a spherical object filled with iron, which most closely reflects the *in vivo* configuration of the contrast agent accumulation, is approximately 10-fold smaller compared with an infinite cylindrical phantom having the same radius and filled with the same substance. Furthermore, the diameter of the *in vivo* sphere is much smaller than the cylindrical phantom, resulting in a smaller magnetic field perturbation. The phantom in this study does not mimic the *in vivo* angiogenesis situation. However, this phantom induces geometrically well-defined susceptibility gradients and therefore it was able to show how positive contrast was induced by white marker and SGM.

4.3. Comparison of different MRI techniques

The analysis was performed on the EVs, which were selected separately for each technique. This selection criterion was chosen to avoid spatial mismatching as positive contrast manifests themselves in different regions and levels for the different techniques. Even with the relatively low iron concentration of 29 μmol Fe kg^{-1} body weight, the *in vivo* CNR for SGM was still greater than 5, which is assumed to be the lower detection limit for molecular imaging (30). The high relaxivities of SPIOs have the opportunity to induce stronger contrast at higher concentrations, which was shown by Zhang *et al.* (6), who used a more than 30 times higher concentration than in the present study. White marker did not show positive contrast in tumor areas where contrast was observed with R_2^* mapping, GE or SGM (Fig. 4). The absence of *in vivo* positive contrast for white marker might be explained as follows. White marker gives positive contrast when a gradient field in the slice direction compensates for the refocusing gradient. Magnetic fields with non-matching strengths or directions will not contribute to the refocusing of the spins. Matching of this gradient field depends on three parameters: the strength of the refocusing gradient, the echo time and the strength of the additional field induced by the iron oxide. This field is derived from the susceptibility gradient, which means that only a part of the gradient will contribute to an effective rephasing. Probably this contribution is too small to be detected *in vivo*. Recently, Varma *et al.* (31) introduced a white marker post-processing approach with a three-dimensional (3D) acquisition, which might resolve these issues.

Small voxel sizes are preferred to measure the spatial pattern of susceptibility effects, because they minimize the contribution of intravoxel dephasing as much as possible. To obtain small voxels a 3D acquisition with isotropic voxels can be used, with the advantage of calculating three susceptibility gradients with SGM and a higher signal-to-noise ratio, compared with a two-dimensional (2D) acquisition. However, the acquisition time of a 3D acquisition is longer and an extra phase-encoding is involved, which is prone to motion artifacts. In this study, a 2D GE acquisition was therefore chosen to achieve a reasonable acquisition time for the *in vivo* experiments. With this 2D

Table 3. Characteristics of the applied susceptibility imaging techniques

	R_2^* mapping	White marker	SGM
Physical principle of contrast	T_2^* shortening	ΔB_z	$\Delta G_{x,y,z}$
Directional sensitivity	No	Yes	Yes
2D and/or 3D	2D and 3D	2D only[a]	2D and 3D
Anatomical information	Yes	No or reduced	Yes
Acquisition time (s)	5×144[b]	144	144

[a]A 3D acquisition can be used for white marker post-processing.
[b]Five different echo times were used for R_2^* mapping.

acquisition, SGM provided promising results and a reasonable CNR *in vivo*. The characteristic properties of all three techniques evaluated in this study are summarized in Table 3.

4.4. Limitations

The plasma half-life of both SPIO contrast agents was approximately 63 s. The amount of homing of a labeled SPIO contrast agent to the vascular target is probably lower compared with other targeted contrast agent with longer plasma half-life owing to the rapid uptake into the reticuloendothelial system, but further histology and biodistribution measurements are needed to substantiate this hypothesis. Despite the short plasma half-life, linear regression analysis in the rim region showed significant differences between labeled and unlabeled SPIOs (Fig. 6). In addition, as a result of the short plasma half-life, post-contrast imaging could be started 10 min after contrast injection and a good target-to-background ratio was achieved. Furthermore, histological validation was performed on a few slices only, since the homing of cNGR conjugated to different particles was already previously validated by histology by different research groups (18,22,32).

4.5. Clinical perspective

Positive contrast techniques using SPIO contrast agents, especially SGM, have a number of potential clinical advantages for future molecular MRI. SGM produces positive contrast images, which are preferred in the reading of radiological images. These SGM images are comparable to GE images in terms of CNR and acquisition time. This is important because eventual clinical implementation of molecular MRI requires rapid imaging techniques. Furthermore, iron oxide particles have already been applied in humans in clinical trials (33).

5. CONCLUSION

This experimental study shows the *in vivo* efficacy of positive contrast imaging techniques for molecular MRI using a cNGR-SPIO contrast agent targeted to the angiogenic vasculature of murine tumors. Of the positive contrast imaging techniques evaluated, SGM is the most promising for molecular imaging. Further research is required to optimize the imaging technique and the design of the iron oxide particles before translation to clinical trials can be made.

Acknowledgments

The authors would like to thank Ludwig Dubois for *in vitro* growth of the tumor cell line and Roel Straathof for performing the dynamic light scattering experiments.

REFERENCES

1. Massoud TF, Gambhir SS. Molecular imaging in living subjects: seeing fundamental biological processes in a new light. Genes Dev 2003; 17(5): 545–580.
2. Gore JC, Yankeelov TE, Peterson TE, Avison MJ. Molecular imaging without radiopharmaceuticals? J Nucl Med 2009; 50(6): 999–1007.
3. Mulder WJ, Strijkers GJ, van Tilborg GA, Cormode DP, Fayad ZA, Nicolay K. Nanoparticulate assemblies of amphiphiles and diagnostically active materials for multimodality imaging. Acc Chem Res 2009; 42(7): 904–914.
4. Aime S, Cabella C, Colombatto S, Geninatti Crich S, Gianolio E, Maggioni F. Insights into the use of paramagnetic Gd(III) complexes in MR-molecular imaging investigations. J Magn Reson Imaging 2002; 16(4): 394–406.
5. Artemov D. Molecular magnetic resonance imaging with targeted contrast agents. J Cell Biochem 2003; 90(3): 518–524.
6. Zhang C, Jugold M, Woenne EC, Lammers T, Morgenstern B, Mueller MM, Zentgraf H, Bock M, Eisenhut M, Semmler W, Kiessling F. Specific targeting of tumor angiogenesis by RGD-conjugated ultrasmall superparamagnetic iron oxide particles using a clinical 1.5-T magnetic resonance scanner. Cancer Res 2007; 67(4): 1555–1562.
7. Seppenwoolde JH, Viergever MA, Bakker CJ. Passive tracking exploiting local signal conservation: the white marker phenomenon. Magn Reson Med 2003; 50(4): 784–790.
8. Mani V, Briley-Saebo KC, Itskovich VV, Samber DD, Fayad ZA. Gradient echo acquisition for superparamagnetic particles with positive contrast (GRASP): sequence characterization in membrane and glass superparamagnetic iron oxide phantoms at 1.5T and 3T. Magn Reson Med 2006; 55(1): 126–135.
9. Cunningham CH, Arai T, Yang PC, McConnell MV, Pauly JM, Conolly SM. Positive contrast magnetic resonance imaging of cells labeled with magnetic nanoparticles. Magn Reson Med 2005; 53(5): 999–1005.
10. Dharmakumar R, Koktzoglou I, Li D. Generating positive contrast from off-resonant spins with steady-state free precession magnetic resonance imaging: theory and proof-of-principle experiments. Phys Med Biol 2006; 51(17): 4201–4215.
11. Stuber M, Gilson WD, Schar M, Kedziorek DA, Hofmann LV, Shah S, Vonken EJ, Bulte JW, Kraitchman DL. Positive contrast visualization of iron oxide-labeled stem cells using inversion-recovery with ON-resonant water suppression (IRON). Magn Reson Med 2007; 58(5): 1072–1077.
12. Dahnke H, Liu W, Herzka D, Frank JA, Schaeffter T. Susceptibility gradient mapping (SGM): a new postprocessing method for positive contrast generation applied to superparamagnetic iron oxide particle (SPIO)-labeled cells. Magn Reson Med 2008; 60(3): 595–603.
13. Mills PH, Ahrens ET. Enhanced positive-contrast visualization of paramagnetic contrast agents using phase images. Magn Reson Med 2009; 62(5): 1349–1355.

14. Liu W, Dahnke H, Jordan EK, Schaeffter T, Frank JA. In vivo MRI using positive-contrast techniques in detection of cells labeled with superparamagnetic iron oxide nanoparticles. NMR Biomed 2008; 21(3): 242–250.
15. Gupta T, Virmani S, Neidt TM, Szolc-Kowalska B, Sato KT, Ryu RK, Lewandowski RJ, Gates VL, Woloschak GE, Salem R, Omary RA, Larson AC. MR tracking of iron-labeled glass radioembolization microspheres during transcatheter delivery to rabbit VX2 liver tumors: feasibility study. Radiology 2008; 249(3): 845–854.
16. Arap W, Pasqualini R, Ruoslahti E. Cancer treatment by targeted drug delivery to tumor vasculature in a mouse model. Science 1998; 279(5349): 377–380.
17. Pasqualini R, Koivunen E, Kain R, Lahdenranta J, Sakamoto M, Stryhn A, Ashmun RA, Shapiro LH, Arap W, Ruoslahti E. Aminopeptidase N is a receptor for tumor-homing peptides and a target for inhibiting angiogenesis. Cancer Res 2000; 60(3): 722–727.
18. Curnis F, Arrigoni G, Sacchi A, Fischetti L, Arap W, Pasqualini R, Corti A. Differential binding of drugs containing the NGR motif to CD13 isoforms in tumor vessels, epithelia, and myeloid cells. Cancer Res 2002; 62(3): 867–874.
19. Di Matteo P, Curnis F, Longhi R, Colombo G, Sacchi A, Crippa L, Protti MP, Ponzoni M, Toma S, Corti A. Immunogenic and structural properties of the Asn–Gly–Arg (NGR) tumor neovasculature-homing motif. Mol Immunol 2006; 43(10): 1509–1518.
20. Colombo G, Curnis F, De Mori GM, Gasparri A, Longoni C, Sacchi A, Longhi R, Corti A. Structure–activity relationships of linear and cyclic peptides containing the NGR tumor-homing motif. J Biol Chem 2002; 277(49): 47891–47897.
21. Buehler A, van Zandvoort MA, Stelt BJ, Hackeng TM, Schrans-Stassen BH, Bennaghmouch A, Hofstra L, Cleutjens JP, Duijvestijn A, Smeets MB, de Kleijn DP, Post MJ, de Muinck ED. cNGR: a novel homing sequence for CD13/APN targeted molecular imaging of murine cardiac angiogenesis in vivo. Arterioscler Thromb Vasc Biol 2006; 26(12): 2681–2687.
22. Oostendorp M, Douma K, Hackeng TM, Dirksen A, Post MJ, van Zandvoort MA, Backes WH. Quantitative molecular magnetic resonance imaging of tumor angiogenesis using cNGR-labeled paramagnetic quantum dots. Cancer Res 2008; 68(18): 7676–7683.
23. Oostendorp M, Douma K, Wagenaar A, Slenter JM, Hackeng TM, van Zandvoort MA, Post MJ, Backes WH. Molecular magnetic resonance imaging of myocardial angiogenesis after acute myocardial infarction. Circulation 2010; 121(6): 775–783.
24. Artemov D, Mori N, Okollie B, Bhujwalla ZM. MR molecular imaging of the Her-2/neu receptor in breast cancer cells using targeted iron oxide nanoparticles. Magn Reson Med 2003; 49(3): 403–408.
25. Vonken EJ, Schar M, Stuber M. Positive contrast visualization of nitinol devices using susceptibility gradient mapping. Magn Reson Med 2008; 60(3): 588–594.
26. Rorden C, Brett M. Stereotaxic display of brain lesions. Behav Neurol 2000; 12(4): 191–200.
27. de Lussanet QG, Beets-Tan RG, Backes WH, van der Schaft DW, van Engelshoven JM, Mayo KH, Griffioen AW. Dynamic contrast-enhanced magnetic resonance imaging at 1.5 Tesla with gadopentetate dimeglumine to assess the angiostatic effects of anginex in mice. Eur J Cancer 2004; 40(8): 1262–1268.
28. Padhani AR. Functional MRI for anticancer therapy assessment. Eur J Cancer 2002; 38(16): 2116–2127.
29. de Lussanet QG, Backes WH, Griffioen AW, van Engelshoven JM, Beets-Tan RG. Gadopentetate dimeglumine versus ultrasmall superparamagnetic iron oxide for dynamic contrast-enhanced MR imaging of tumor angiogenesis in human colon carcinoma in mice. Radiology 2003; 229(2): 429–438.
30. Oostendorp M, Post MJ, Backes WH. Vessel growth and function: depiction with contrast-enhanced MR imaging. Radiology 2009; 251(2): 317–335.
31. Varma G, Pedersen SF, Taupitz M, Botnar RM, Dahnke H, Keevil SF, Schaeffter T. Utilizing different methods for visualizing susceptibility from a single multi-gradient echo dataset. MAGMA 2009; 22(5): 297–308.
32. Pastorino F, Brignole C, Di Paolo D, Nico B, Pezzolo A, Marimpietri D, Pagnan G, Piccardi F, Cilli M, Longhi R, Ribatti D, Corti A, Allen TM, Ponzoni M. Targeting liposomal chemotherapy via both tumor cell-specific and tumor vasculature-specific ligands potentiates therapeutic efficacy. Cancer Res 2006; 66(20): 10073–10082.
33. Lahaye MJ, Engelen SM, Kessels AG, de Bruine AP, von Meyenfeldt MF, van Engelshoven JM, van de Velde CJ, Beets GL, Beets-Tan RG. USPIO-enhanced MR imaging for nodal staging in patients with primary rectal cancer: predictive criteria. Radiology 2008; 246(3): 804–811.

